Supporting information for

Copper complexes as bioinspired models for Lytic Polysaccharide Monooxygenases

Alda Lisa Concia, Maria Rosa Beccia, Maylis Orio, Francine Terra Ferre, Marciela Scarpellini, Frédéric Biaso, Bruno Guigliarelli, Marius Réglier, A. Jalila Simaan

I. Experimental section

General procedures

Chemicals were obtained from commercial sources and used without further purification. CAUTION! Perchlorate salts are potentially explosive. Only a small amount of material should be prepared and handled with care.

ESI-MS analyses were performed using a SYNAPT G2 HDMS (Waters) spectrometer equipped with a pneumatically assisted Atmospheric Pressure Ionization (API) source. The ion-spray voltage was 2.8 kV, the orifice lens was 20 V, and the nitrogen flux (nebulization) was 100 L h^{-1}. The HR mass spectra were obtained with a time-of-flight (TOF) analyzer. The sample was placed in a methanol/0.1 mM sodium chloride solution or 3mM ammonium acetate. The results were validated by three measurements.

Elemental analysis were performed using a Thermo Finnigan EA 1112 instrument. The results were validated by at least two measurements. FT-IR spectra were recorded in attenuated total reflection (ATR) mode on a Bruker TENSOR 27 spectrometer equipped with a single-reflection DuraSamplIR diamond ATR accessory. NMR spectra were recorded on a Brucker-Avance III nanobay spectrometer (300 or 400 MHz) using TMS as internal reference.

Syntheses of (L^{IM})

2-(2-Amino-ethyl)pyridine (0.56 g, 4.58 mmol) and 1-methyl-2-imidazolecarboxaldehyde (0.50 g, 4.58 mmol) were refluxed in anhydrous methanol (50 ml) overnight. The resulting solution was dried under reduced pressure to yield dark yellow oil (quantitative yield). ^{1}H NMR (400 MHz, CDCl$_3$) δ 8.52 (dd, J = 4.8, 0.7 Hz, 1H), 8.24 (s, 1H), 7.55 (td, J = 7.7, 1.8 Hz, 1H), 7.15 (d, J = 7.8 Hz, 1H), 7.11 – 7.06 (m, 1H), 7.05 (d, J = 0.9 Hz, 1H), 6.87 (s, 1H), 3.97 (td, J = 7.0, 1.0 Hz, 2H), 3.88 (s, 3H), 3.14 (t, J = 7.1 Hz, 2H). ^{13}C NMR (75 MHz, CDCl$_3$) δ 159.8 (C), 153.6 (CH), 149.5 (CH), 143.2 (C), 136.3 (CH), 129.2 (CH), 124.8 (CH), 123.5 (CH), 121.4 (CH), 61.4 (CH$_2$), 39.8 (CH$_2$), 35.3 (CH$_3$).

Syntheses of (L^{AM})

(L^{IM}) (0.80 g, 3.73 mmol) was dissolved in anhydrous methanol (50 ml) and cooled to 0°C. NaBH$_4$ (0.21 g, 5.6 mmol) was added slowly and the reaction mixture was warmed up to room temperature. After 5 hours, the solvent was removed under reduced pressure. The crude

was dissolved in 10% $NaHCO_3$ solution and extracted with dichloromethane. The organic phases were collected, washed with brine and dried over anhydrous sodium sulfate. The solvent was evaporated under vacuum and a dense yellow oil was obtained (0.630 g, yield 78%). ^{1}H NMR (400 MHz, $CDCl_3$) δ 8.49 (d, J = 4.2 Hz, 1H), 7.56 (td, J = 7.7, 1.8 Hz, 1H), 7.14 (d, J = 7.8 Hz, 1H), 7.11 − 7.06 (m, 1H), 6.89 (d, J =0.9 Hz, 1H), 6.78 (d, J =0.8 Hz, 1H), 3.87 (s, 2H), 3.61 (s, 3H), 3.09 − 2.94 (m, 4H), 2.55 (brs, 1H). ^{13}C NMR (101 MHz, $CDCl_3$) δ 160.1 (C), 149.3 (CH), 146.2 (C), 136.6 (CH), 127.15 (CH), 123.4 (CH), 121.4 (2CH), 49.0 (CH_2), 45.5 (CH_2), 38.0 (CH_2), 32.8 (CH_3).

Synthesis of complex $[(L^{AM})Cu(CH_3CN)](ClO_4)_2$ (**1**).

The ligand (L^{AM}) (2.31 mmol, 0.500 g) was dissolved in 10 ml of methanol and a water solution (3 ml) of copper(II) perchlorate hexahydrate (2.31, 0.856 g) was added slowly under stirring. The resulting deep blue solution was stirred for 1 hour and the solvents were slowly evaporated. Recrystallization in acetonitrile provided suitable crystals for X-Ray diffraction analysis (yield 50%). Elemental analysis calcd (%) for $C_{14}H_{19}Cl_2CuN_5O_8$: C 32.25, H 3.68, N 13.47 ; found: C 32.25, H 3.55, N 13.12. *ESI-MS* $C_{12}H_{16}N_4O_8Cl_2Cu$ *m/z* [M+Na][+] calcd: 499.9533; found: 499.9521. UV/Vis (methanol): λ_{max}/nm(ε /mol[−1]Lcm[−1]) = 262 (6750), 660 (82). UV/Vis (water): λ_{max}/nm (ε/ mol[−1]Lcm[−1]) = 260 (5400), 660 (56). FT-IR (ν/cm[−1]): 3238, 1612, 1514, 1442, 1168, 1067, 763, 618.

Synthesis of complex $[(L^{IM})Cu(OH_2)](ClO_4)_2 \cdot H_2O$ (**2**).

The ligand (L^{IM}) (2.33 mmol, 0.500 g) was dissolved in 10 ml of methanol and a water solution (5 ml) of copper(II) perchlorate hexahydrate (2.33, 0.860 g) was added slowly under stirring. The resulting deep blue solution was stirred for 1 hour. Then, the solution was let stand at room temperature until crystals suitable for crystallographic analysis were formed (yield 55%). Elemental analysis calcd (%) for $C_{12}H_{18}Cl_2CuN_4O_{10}$: C 28.11, H 3.54, N 10.93; found: C 28.01, H 3.47, N 10.79. ESI-MS $C_{12}H_{14}N_4O_8Cl_2Cu$ *m/z* [M+Na][+] calcd: 497.9377; found 497.9366. UV/Vis (methanol): λ_{max}/nm (ε/mol[−1]Lcm[−1]) = 259 (12900), 299 (9340), 665 (76). UV/Vis (water): λ_{max}/nm (ε/ mol[−1]Lcm[−1]) = 258 (7000), 300 (6000), 660 (60). FT-IR (ν/cm[−1]) 1633, 1610, 1504, 1444, 1066, 777, 620.

Synthesis of $[(L^{IM})_2Cu_2](PF_6)_2$

Under inert atmosphere the ligand L^{IM} (1.17 mmol, 0.250 g) was dissolved in dry acetonitrile previously purged with N_2. A solution of copper(I) tetrakis(acetonitrile) hexafluorophosphate

(1.17 mmol, 0.434 g) in the same solvent was slowly added and the solution turned from yellow to brown. After stirring during one hour, the mixture was kept under inert atmosphere and crystals suitable for crystallographic analysis were formed.

Crystallographic structure determination

Suitable crystals were measured on a Rigaku Oxford Diffraction SuperNova diffractometer at 293K using the CuKα radiation (λ=1.54184 Å). Data collection reduction and multiscan ABSPACK correction were performed with CrysAlisPro (Rigaku Oxford Diffraction). The structures were solved by direct methods with SHELXS and SHELXL[1] was used for full matrix least squares refinement. All H-atoms were found experimentally and their coordinates and Uiso parameters were constraint to 1.5Ueq (parent atoms) for the methyls and to 1.2Ueq (parent atom) for the other carbons. Crystal structure(s) have been deposited at the Cambridge Crystallographic Data Centre with the following deposition numbers 1476062 (**2**); 1476063 (**1**) and 1516144 ($[(L^{IM})_2Cu_2](PF_6)_2$)

Cyclic voltammetry

Cyclic voltammetry experiments were recorded on a Biologic SP-150 potentiostat using a conventional three-electrode system (each compartment is separated by a porous bridge) consisting of a glassy carbon (2 mm^2) working electrode, a platinum wire counter electrode and an AgCl/Ag reference electrode. Experiments were conducted at 0.1 V·s^{-1} in a 5 mL electrochemical cell equipped with an argon-purge system, at room temperature. The complexes were placed at 2 mM concentrations in water containing 0.1 M of $NaNO_3$. The potential of the ferricyanide/ferrocyanide couple was measured at 0.193 V in our set-up and this potential was used to calculate the potentials *vs*. Standard Hydrogen Electrode (SHE).[2] Alternatively, the complexes were placed at 2 mM concentrations in dry MeOH containing 0.1 M of Bu_4NClO_4. All the potentials in the text are therefore given *vs*. SHE.

Redox titration

Midpoint redox potentials of **1** and **2** were determined by potentiometric titration at pH 6 in 0.1 M of 2-(*N*-morpholino)ethanesulfonic acid (MES) buffer followed by EPR spectroscopy. Titrations were performed at room temperature in an anaerobic glove-box ($O_2 < 2$ ppm). Redox potentials were adjusted with small additions of sodium dithionite and measured with a combined Pt-Ag/AgCl/KCl (3M) Mettler-Toledo micro-electrode calibrated by using redox

buffer solutions and are given in the text with respect to the standard hydrogen electrode. The following redox mediators were used at 10 μM final concentrations for all titrations: 1,1'-ferrocene dimethanol; ferrocene; *N,N*-dimethyl-*p*-phenyldiamine; 1,4-benzoquinone; dichlorophenolindophenol; 1,2-naphtoquinone; phenazine ethosulfate. For EPR spectroscopy, samples were anaerobically transferred into calibrated EPR tubes that were rapidly frozen in glove box.

EPR spectroscopy

EPR spectra were collected at X-band (9.4 GHz) using a Bruker ELEXSYS E500 spectrometer, with a standard rectangular Bruker (ST) cavity equipped with an Oxford Instruments ESR 900 helium flow cryostat. Measurements were performed at 0.51 mW microwave power, 1.6 mT modulation amplitude and a temperature of 50 K. For *g*-values determination, magnetic field values were corrected against a known g standard (weak pitch, $g = 2.0028 \pm 0.0001$).

Oxidation of *p*-nitrophenyl-β-D-glucopyranoside

Activity assays were performed in total volume of 300 μL placed in 96-well plates. Complexes **1** or **2** were solubilized at concentration ranging from 0.01 to 0.6 mM in aqueous solutions (either water or phosphate buffer 10 mM pH 7 or carbonate buffer 100 mM at pH 10.5). The substrate *p*-nitrophenyl-β-D-glucopyranoside was used at concentrations of 5-40 mM and hydrogen peroxide at concentrations of 3-30 mM. Controls were performed using the same conditions, but in the absence of complexes or hydrogen peroxide or the substrate alone in similar reaction conditions. Controls were also performed in the presence of $CuSO_4.5H_2O$ instead of the complexes. Reaction mixtures were incubated at 30°C and were monitored by following the absorbance at 400 nm using a BioTek Synergy MX microplate reader. Initial velocities were extracted from the slopes during the first 10 minutes of reaction in carbonate buffer at pH 10.5. Quantification was performed measuring the absorbance at 400 nm ($\varepsilon=$ 18500 $mol^{-1}Lcm^{-1}$) and using calibration curves obtained with commercial *p*-nitrophenol placed at different pHs. When performed in water, the amount of *p*-nitrophenolate was determined at the end of the reaction after basification of the medium by addition of carbonate buffer at pH 10.5 to reach a final concentration of 100 mM.

For the successive addition of hydrogen peroxide, the complex was at a concentration of 0.05 mM (in carbonate buffer 100 mM at pH 10.5) in the presence of 20 mM of *p*-nitrophenyl-β-D-glucopyranoside. 15 mM of hydrogen peroxide were added every 2 h during 10 h (5 successive additions). The product *p*-nitrophenolate was quantified spectrophotometrically as described above after 24 h.

DFT-calculations

All theoretical calculations were performed with the ORCA program package.[3] Full geometry optimizations were undertaken for all complexes using the GGA functional BP86[4] and by taking advantage of the resolution of the identity (RI) approximation in the Split-RI-J variant[5] with the appropriate Coulomb fitting sets[6] Scalar relativistic effects were included with ZORA paired using the SARC def2-TZVP(-f) basis sets[7,8] and the decontracted def2-TZVP/J Coulomb fitting basis sets for all atoms. Increased integration grids (Grid4 and GridX4 in ORCA convention) and tight SCF convergence criteria were used. Electronic structures and Molecular Orbital diagrams were obtained from single-point calculations using the hybrid functional B3LYP[9]. Increased integration grids (Grid4 and GridX4 in ORCA convention) and tight SCF convergence criteria were used in the calculations. For according to the experimental conditions solvent effects were accounted and water was used as solvent ($\varepsilon = 80$) within the framework of a dielectric continuum approach: the conductor-like screening model (COSMO).[10] EPR parameters were evaluated from additional single point calculations using the B3LYP functional. Picture change effects were applied and the integration grids were increased to an integration accuracy of 11 (ORCA convention) for the metal center. Optical properties were also predicted from additional single-point calculations using the hybrid functional B3LYP. Electronic transition energies and dipole moments for all models were calculated using time-dependent DFT (TDDFT)[11] within the Tamm–Dancoff approximation.[12] To increase computational efficiency, the RI approximation[13] was used in calculating the Coulomb term, and at least 30 excited states were calculated in each case. For each transition, difference density plots were generated using the ORCA plot utility program and were visualized with the Chemcraft program.[14]

II. Crystallographic data

Selected crystallographic data

Table S 1. Selected crystallographic data for complexes **1, 2** and **[(L^{IM})$_2$Cu$_2$](PF$_6$)$_2$**

Compound	1	2	[(L^{IM})$_2$Cu$_2$](PF$_6$)$_2$
Formula	C$_{14}$H$_{19}$Cl$_2$CuN$_5$O$_8$	C$_{12}$H$_{18}$Cl$_2$CuN$_4$O$_{10}$	C$_{12}$H$_{14}$CuF$_6$N$_4$P
M$_w$	519.78	512.74	422.78
Crystal system	triclinic	triclinic	triclinic
Measurement temperature/ K	293	293	223.00
Space group	P -1	P -1	P-1
a/ Å	8.8001(3)	8.1405(3)	8.8213(3)
b/ Å	10.4679(3)	10.3453(4)	9.0761(3)
c/ Å	11.3132(3)	11.6756(4)	9.9917(4)
α/ °	84.583(2)	85.809(3)	85.611(3)
β/ °	79.429(3)	83.461(3)	78.271(3)
χ/ °	83.371(3)	84.995(3)	73.584(3)
V/ Å^3	1014.75(5)	971.18(7)	751.17(5)
Z	2	2	2
Dc/g.cm^{-3}	1.701	1.753	1.869
Crystal colour	blue	blue	brown
Crystal size/mm^3	0.18×0.16×0.08	0.24×0.15×0.05	0.22×0.22×0.1
μ/mm^{-1} (Cu-Kα)	4.438	4.69	3.759
N° of refl. measured	6307	13096	10225
N° of unique refl.	4034	3370	2916
N° of observed refl.[F^2 > 4σF^2]	3806	3033	2705
N° parameters refined	273	265	217
R$_1$ [F^2>4σF^2]	0.0330	0.0362	0.0300
wR$_1$ [F^2>4σF^2]	0.0911[b]	0.0928[a]	0.0779
R$_2$ [all refl.]	0.0344	0.0405	0.0326
wR$_2$ [all refl.]	0.0925	0.0070	0.0801
Goodness of fit [all refl.]	1.063	1.036	1.056
Residual Fourier/e. Å^{-3}	-0.388; 0.427	-0.294; 0.401	-0.375; 0.416
CCDC	**1476063**	**1476062**	**1516144**

[a] w=1/[σ^2(Fo^2)+(0.0484P)^2+0.8659P] where P=(Fo^2+2Fc^2)/3

[b] w=1/[σ^2(Fo^2)+(0.051P)^2+0.4015P] where P=(Fo^2+2Fc^2)/3

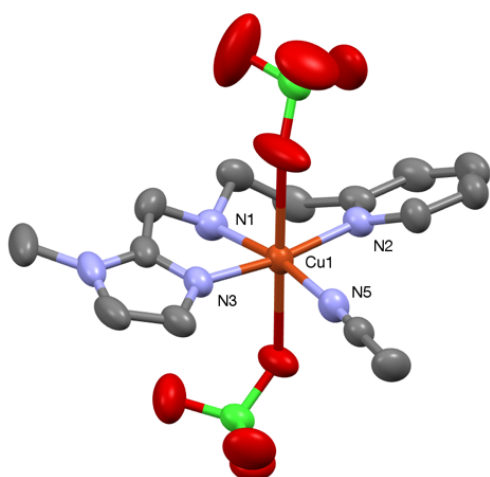[c] w=1/[σ^2(Fo^2)+(0.0389P)^2+0.4648P] where P=(Fo^2+2Fc^2)/3

Structure of complex 1

Figure SI 1. ORTEP diagram of complex **1** (50% thermal ellipsoid plots). Hydrogen atoms were omitted for clarity. Selected distances in Å: Cu1-N1: 2.0322(17), Cu1-N2: 2.0175(17), Cu1-N3: 1.9684(17), Cu1-N5 2.0015(18). Selected angles in deg: N2-Cu1-N1: 95.11(7), N3-Cu1-N1: 80.89(7), N3-Cu1-N5: 89.89(7), N5-Cu1-N2: 94.74(7).[15]
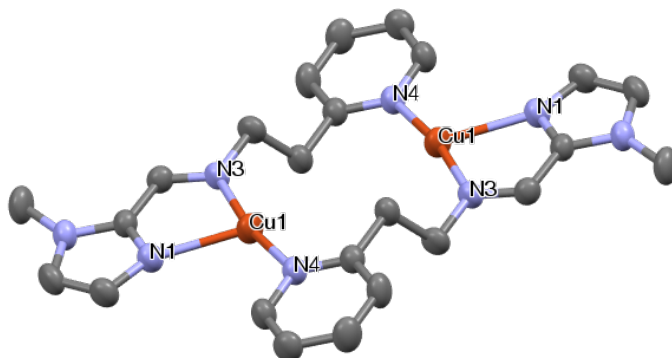
Structure of $[(L^{IM})_2Cu_2](PF_6)_2$

Figure SI 2. ORTEP diagram of complex $[(L^{IM})_2Cu_2](PF_6)_2$ (30% thermal ellipsoid plots). Hydrogen atoms and counter-anions were omitted for clarity. Selected distances in Å: Cu1-N1: 2.2900(17); Cu1-N3: 1.9346(16); Cu1-N4: 1.9165(16). Selected angles in deg: N3-Cu1-N1: 80.81(6), N4-Cu1-N1: 109.15(6), N4-Cu1-N3: 169.57(7).

III. Redox properties of 1 and 2

Cyclic voltammetry in methanol

In the case of complex **2**, the CV curves are characterized by one cathodic peak ($E_p^{c,1}$ = 150 mV vs. NHE) attributed to the reduction of Cu(II) into Cu(I) and one anodic peak ($E_p^{a,1}$ = 310 mV vs. NHE) indicating a "pseudo-reversible" redox process with a difference between the

reduction and oxidation peaks ΔE_p of 160 mV higher than the expected 60 mV for a fully reversible one-electron redox process (see Figure SI 3 and Table S 2). In the case of **1**, a major pseudo-reversible redox process is present ($E_p^{c,1}$ = 160 mV and $E_p^{a,1}$ = 255 vs. NHE) but an additional redox couple appears ($E_p^{c,2}$ = 25 mV and $E_p^{a,0}$ = 98 vs. NHE). The latter redox couple can be either due to an impurity or to the presence of an acetonitrile-coordinated complex.
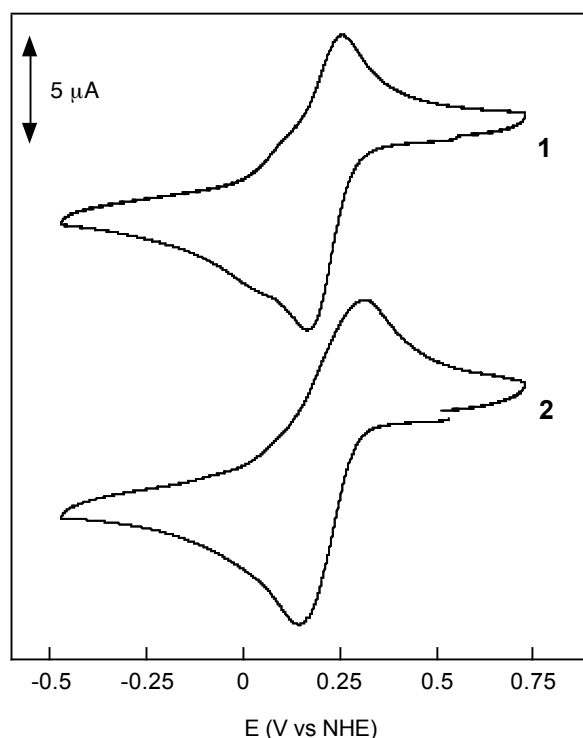

Figure SI 3. Cyclic voltammograms of **1** and **2** placed at 2 mM in methanol containing 0.1 M Bu_4NClO_4. Scan rate = 100 mV.s^{-1}.

Cyclic voltammetry in water

While scanning towards the negative potentials (cathodic scans), the CV curves are characterized by one cathodic peak (E_p^c) attributed to the reduction of Cu(II) into Cu(I) at -47 and -52 mV for complexes **1** and **2** respectively (see Figure SI 4). This also supports the fact that, in the case of **1**, acetonitrile is mainly decoordinated in water since only one reduction peak is observed. On the reverse scan, a major reoxidation peak for **1** is observed at +55 mV indicating a pseudo-reversible redox process with a difference between the reduction and oxidation peaks ΔE_p of 102 mV higher than the expected 60 mV for a fully reversible one-electron redox process. A minor peak is also observed at + 410 mV. In the case of complex **2**,

9

three anodic peaks are observed at + 62 , +210 and +360 mV. In both cases, the presence several anodic peaks suggest that chemical reactions are coupled with the electron transfer and that different Cu(I) complexes co-exist in solution (possibly different conformations or formation of a 'L$_2$Cu$_2$' complex similar to the one that has been crystallized). However, the presence of several Cu(I) species do not lead to major decomposition of the initial complexes since several cycles can be performed without significantly altering the cathodic and anodic peaks. The major reoxidation peak in the case of **2** is at 62 mV (used for the calculation), a value very similar to that of complex **1**. The redox potentials for the Cu(II)/Cu(I) couple in complexes **1** and **2** was therefore calculated and are found around 5 mV *vs*. SHE for both complexes (Table S 3).
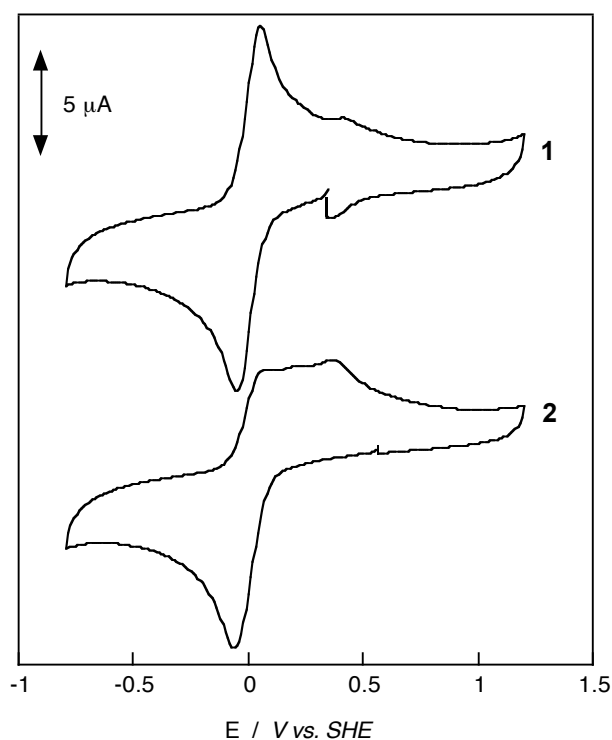
Figure SI 4. Cyclic voltammograms of **1** and **2** placed at 2 mM in H$_2$O containing 0.1 M NaNO$_3$. Scan rate = 100 mV.s^{-1}.

Table S 2. Cathodic and anodic peaks observed by cyclic-voltammetry. Potentials are given in mV vs. NHE

		$E_p^{c,1}$	$E_p^{c,2}$	$E_p^{a,0}$	$E_p^{a,1}$	$E_p^{a,2}$	$E_p^{a,3}$
Methanol	Complex **1**	160	25	98	255	-	-
	Complex **2**	150	-	-	315	-	-
Water	Complex **1**	-47	-	-	+55	-	+410
	Complex **2**	-52	-	-	+64	+210	+360

Redox titrations

Given the complexity of the CV curves, redox titrations monitored by EPR spectroscopy were also performed in buffered solutions (0.1M MES buffer at pH 6) for the two complexes by following the spin intensity of the Cu(II) signals upon reduction with dithionite. In both cases, the spin intensity variations with redox potential were fitted by Nernst curve corresponding to a one-electron redox process. (Figure SI 5). Under these conditions, the midpoint potentials for the Cu(II)/Cu(I) couples in complexes **1** and **2** were found about + 17 mV and + 50 mV *vs*. SHE, respectively. In the case of complex **1**, this value is close to the one recorded from cyclic voltammetry experiments (Table S 3). In the case of complex **2**, a non-negligible difference between the two sets of values was found. It may be related to the different experimental conditions used (pH, buffer) but it can also be related to the presence of different Cu(I) species with different oxidation potentials that are detected in the CV experiment.
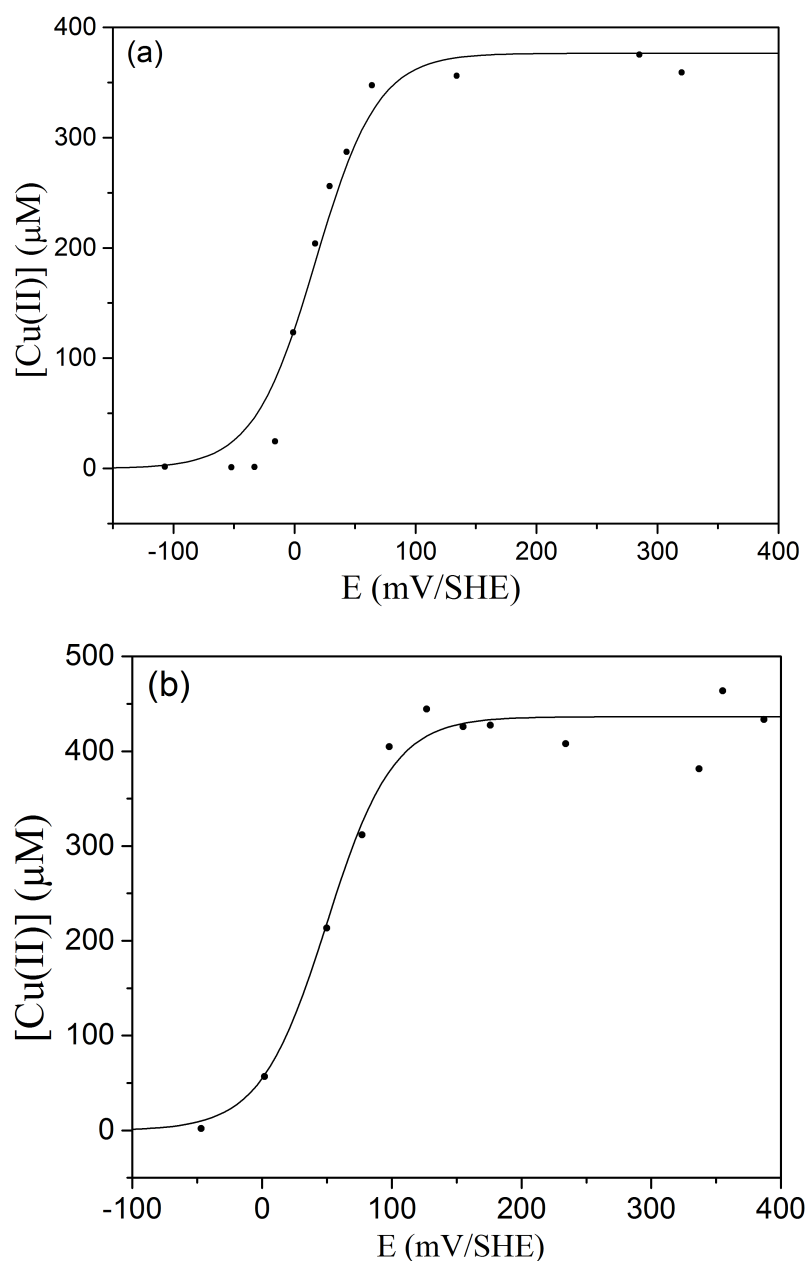
Figure SI 5. Redox titration curves of **1** (top) and **2** (bottom) in 0.1 M of MES buffer at pH 6. Experimental data (points) and fit with a Nernst equation (plain lines) with redox potentials given in table S2.

Table S 3. Redox potentials for the Cu(II) / Cu(I) couples of **1** and **2** expressed in mV *vs*. SHE obtained from cyclic voltammetry (CV) or redox titrations.

	CV (H$_2$O / NaNO$_3$)	Redox titration (H$_2$O MES pH6 / KNO$_3$)
1	5 ± 10	17 ± 10
2	5 ± 10	50 ± 10

IV. Additional data on the reactivity of complexes 1 and 2

Oxidation of p-nitrophenyl-ß-d-glucopyranoside in carbonate buffer at pH 10.5: Effect of complex concentration
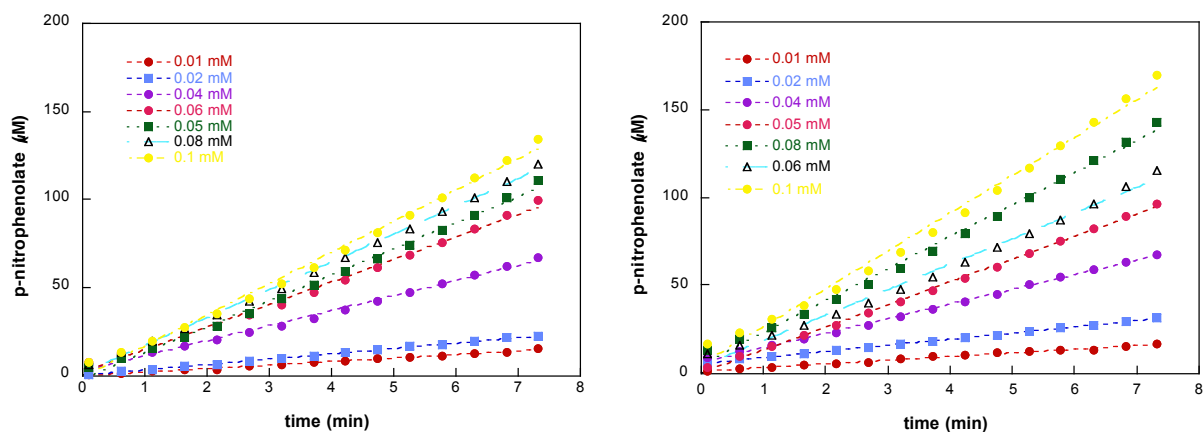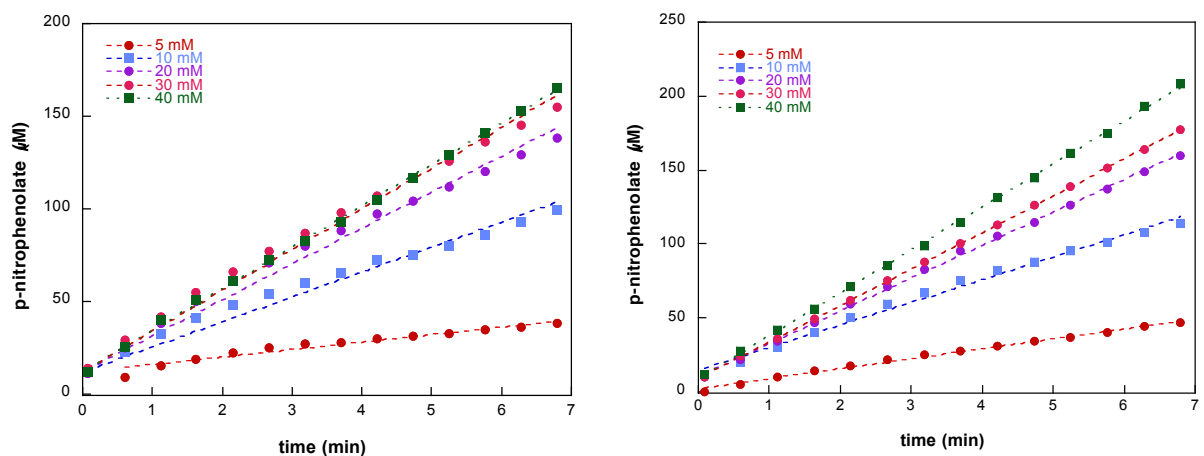

Figure SI 6. Time dependent evolution of the concentration of *p*-nitrophenolate for the reaction of **1** (left) and **2** (right) with *p*-nitrophenyl-β-d-glucopyranoside in carbonate buffer at pH 10.5 with different concentrations of complexes using [S] = 20 mM and [H$_2$O$_2$]=20 mM.

Oxidation of p-nitrophenyl-ß-d-glucopyranoside in carbonate buffer at pH 10.5: Effect of substrate concentration
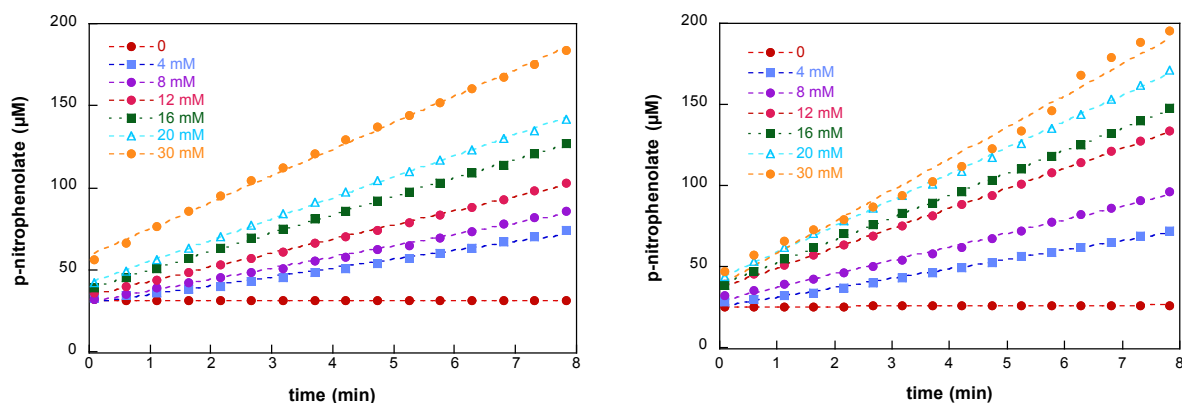

Figure SI 7. Time dependent evolution of the concentration of *p*-nitrophenolate for the reaction of **1** (left) and **2** (right) with *p*-nitrophenyl-β-d-glucopyranoside in carbonate buffer at pH 10.5 with different concentrations of substrate using [**1** or **2**] = 0.2 mM and [H$_2$O$_2$]=20 mM.
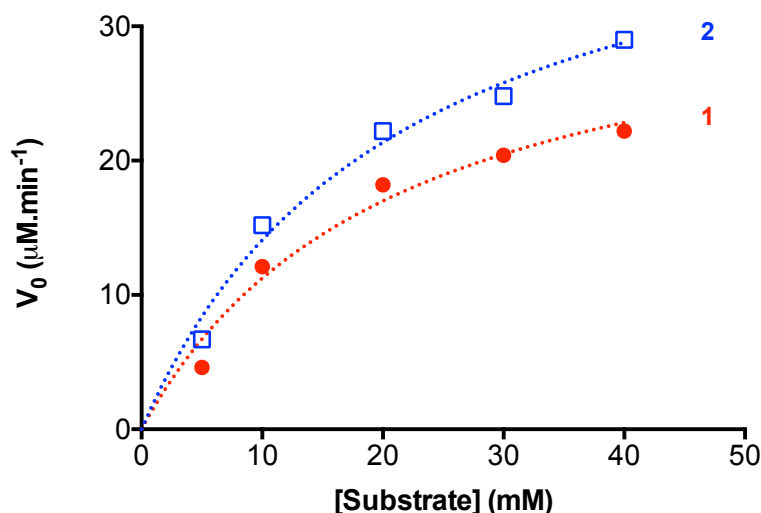
Figure SI 8. Initial rates as a function of the concentration of *p*-nitrophenyl-β-D-glucopyranoside (20 mM) in the presence of hydrogen peroxide in carbonate buffer 100 mM pH 10.5 at 30°C. [**1** or **2**] = 0.2 mM, [H_2O_2]=20 mM. Data have been fitted with Michaelis-Menten model providing K_M= 21 mM for both complexes and Vmax= 35 and 44 $\mu M.min^{-1}$ for **1** and **2** respectively (i.e kcat= 0.17 and 0.22 min^{-1}).

Oxidation of p-nitrophenyl-β-D-glucopyranoside in carbonate buffer at pH 10.5: effect of hydrogen peroxide concentration

Figure SI 9. Time dependent evolution of the concentration of *p*-nitrophenolate for the reaction of **1** (left) and **2** (right) with *p*-nitrophenyl-β-d-glucopyranoside in carbonate buffer at pH 10.5 with different concentrations of hydrogen peroxide using [**1** or **2**] = 0.2 mM and [S]=20 mM.
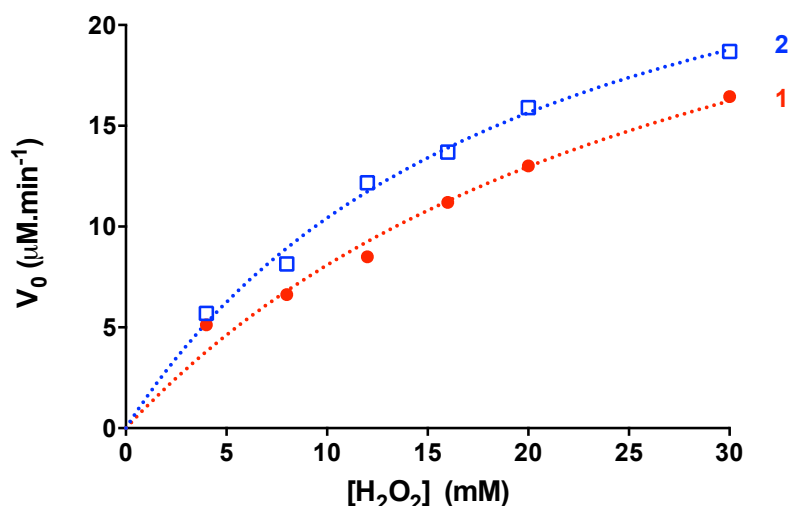
Figure SI 10. Initial rates as a function of hydrogen peroxide concentration for the reaction of complexes **1** and **2** at 0.2 mM concentration with *p*-nitrophenyl-β-D-glucopyranoside (20 mM) in carbonate buffer 100 mM, pH 10.5 and 30°C. Data have been fitted with Michaelis-Menten model providing K_M= 20 and 30 mM (for **1** and **2** respectively) and a similar V_{max}= 30 μM.min^{-1} for both complexes (i.e k_{cat}= 0.15 min^{-1}).

Oxidation of p-nitrophenyl-β-D-glucopyranoside in carbonate buffer at pH 10.5: comparison with copper salt
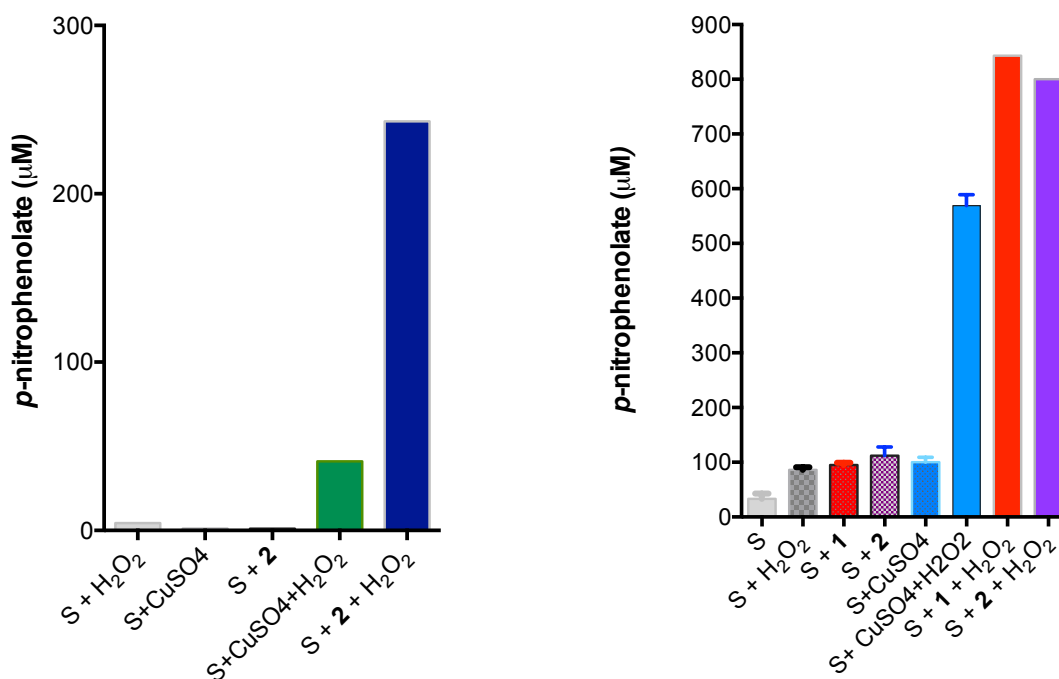
Figure SI 11. Reaction of *p*-nitrophenyl-β-D-glucopyranoside (S) with complexes **1** and **2** or with CuSO$_4$ and H$_2$O$_2$ in carbonate buffer 100 mM pH 10.5 at 30°C using [H$_2$O$_2$]=20 mM and [S] =20 mM. Left: concentration of *p*-nitrophenolate obtained after 10 minutes of reaction with [**1** or **2** or CuSO$_4$]=0.01 mM. Right: concentration of *p*-nitrophenolate obtained after 24 hours of reaction with [**1** or **2** or CuSO$_4$]=0.05 mM.
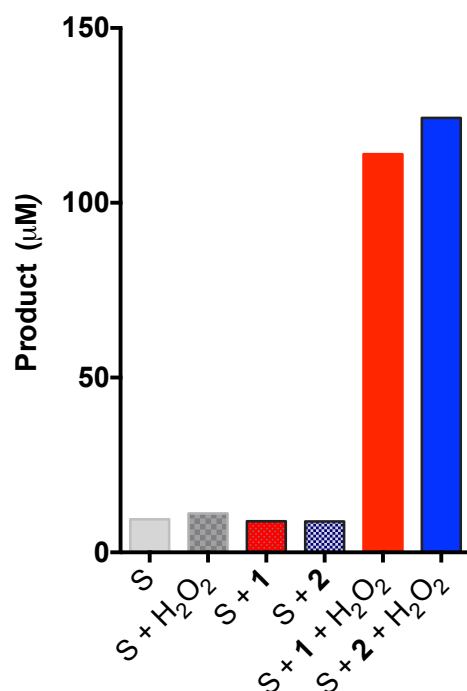
15

Oxidation of p-nitrophenyl-β-D-glucopyranoside in phosphate buffer at pH 7

Figure SI 12. Concentrations of *p*-nitrophenolate obtained after 24 hours of reaction in phosphate buffer set at pH 7 with [**1** or **2**]=0.1 mM, [H_2O_2]=20 mM and [S] =20 mM.

HPAEC-PAD chromatogram of gluconic acid containing fraction after HPLC purification from reaction mixture

Reaction mixtures were purified by preparative HLPC with a reverse phase C18 column (Jupiter 300 Å, 15μm, 250x21.2mm, Phenomenex). Gluconic acid was eluted with 100% water + 0.1% trifluoroacetic acid while *p*-nitrophenol and the excess of *p*-nitrophenyl-β-d-glucopyranoside were eluted with 90% acetonitrile. High-performance Anion-Exchange Chromatography with Pulsed Amperometric Detection (HPAEC-PAD) was conducted using a Dionex system set up with a disposable electrochemical gold electrode, a CarboPac PA1 2×250 mm analytical column (Thermo Scientific, Dionex) and a CarboPac PA1 2×50 mm guard column. HPAEC-PAD analysis of samples was performed following the procedure previously described in literature[16] and commercial gluconic acid as standard (Aldrich).
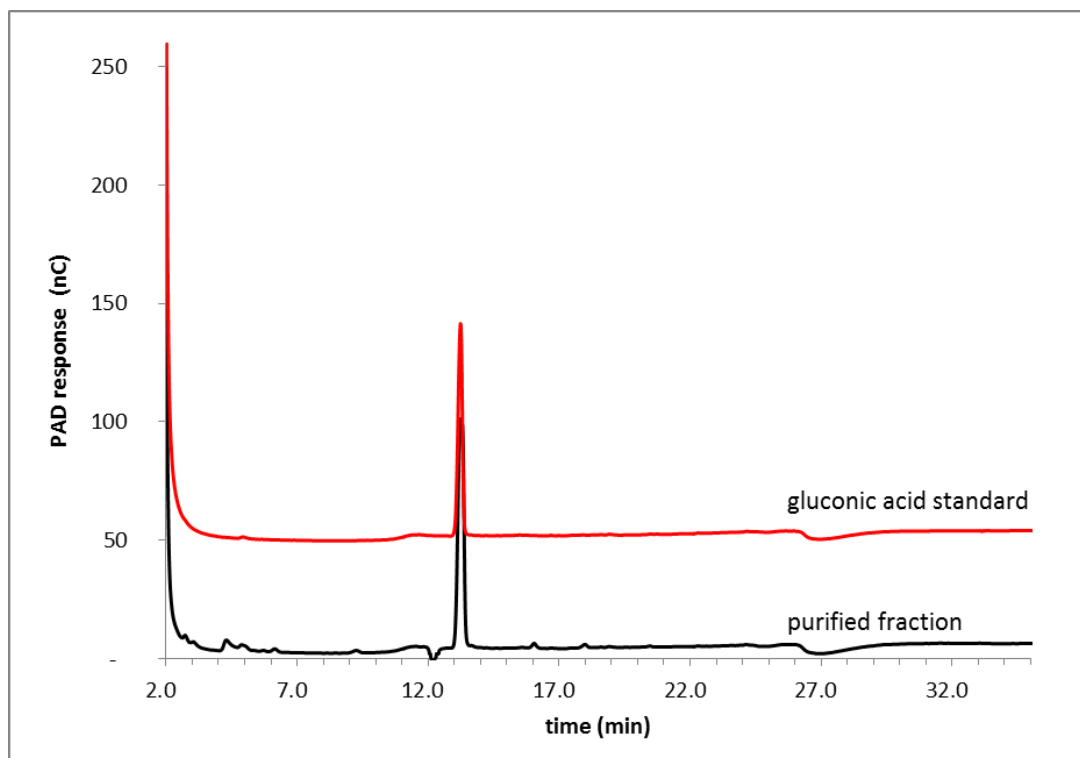
Figure SI 13. HPAEC-PAD analysis of (top) commercial gluconic acid standard (bottom) reaction mixture after purification on preparative-scale HPLC.
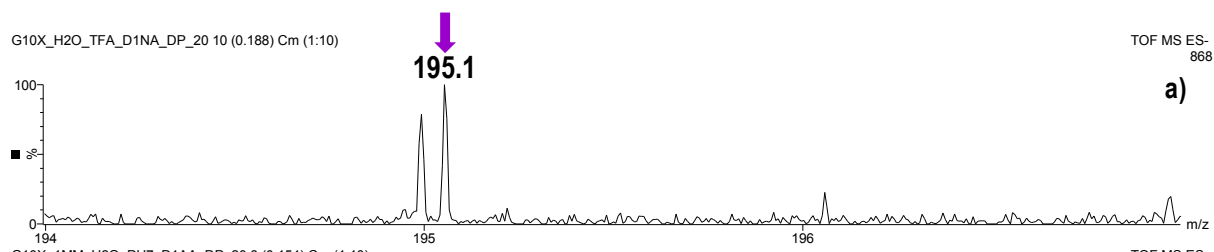
ESI-MS detection of gluconic acid

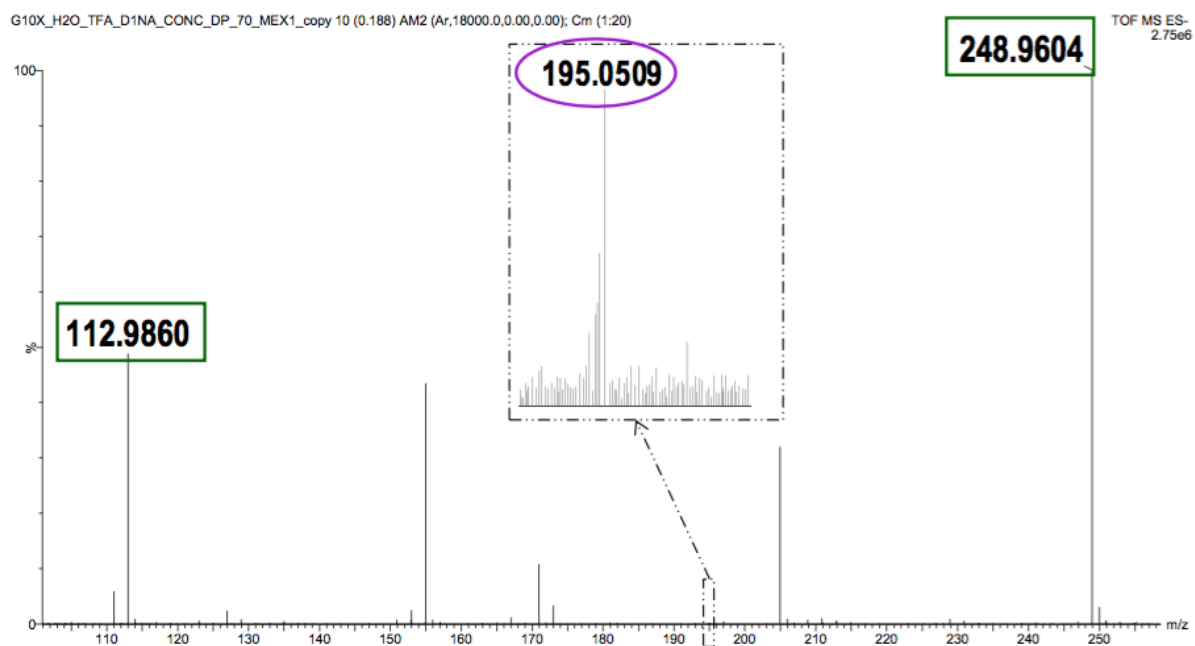Figure SI 14. ESI-MS spectra in negative mode of gluconic acid in the reaction mixture after 24h of reaction.

Figure SI 15. HR-MS spectrum of the reaction mixture after 24h after purification on preparative-scale HPLC. The ion at m/z 195.0509 corresponds to a compound with monoisotopic mass of 196.0583 Da (error < 3 ppm) and is attributed to gluconic acid. Ions at m/z 112.9860 et m/z 248.9604 were used as internal standards (sodium trifluoroacetate conglomerats $(CF_3COONa)_nCF_3COO^-$)).
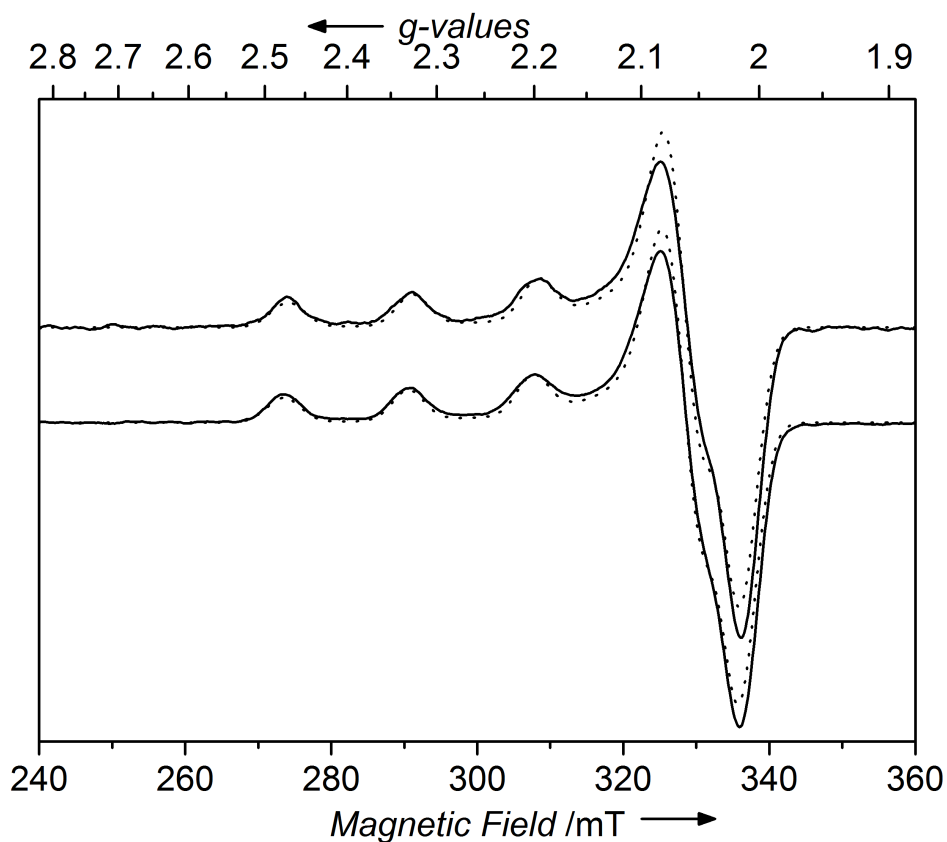
V. EPR Analysis

EPR analysis of 1 and 2

Figure SI 16. X-band continuous wave EPR spectra of **1** (up) and **2** (bottom) with simulations (dotted lines) in aqueous solution (MES buffer pH6).

Table S 4. EPR parameters obtained from simulation for complexes **1** and **2** and of the intermediate in different conditions.

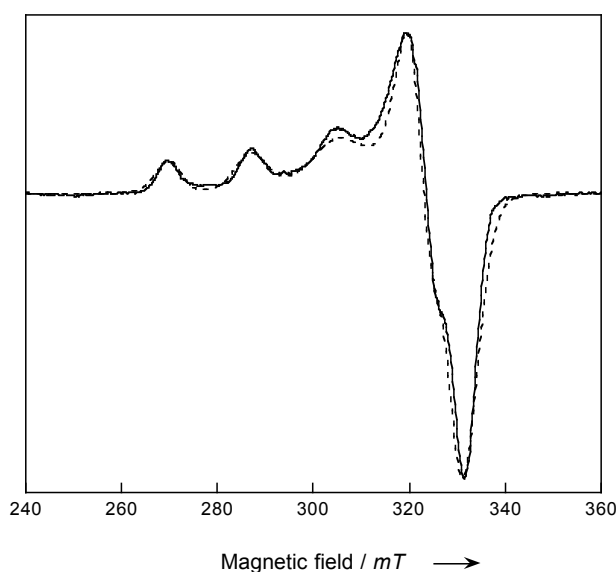|	$g_{//}$	$g_{\perp}$	$|A_{//}|$ in MHz (in Gauss)
1 in MES buffer pH6	2.260	2.059	530 (173)
1 in H_2O	2.258	2.068	535 (172)
1 in MeOH	2.269	2.061	525 (165)
2 in MES buffer pH6	2.265	2.060	530 (167)
2 in H_2O	2.270	2.064	540 (170)
1 + H_2O_2/Et_3N	2.249	2.066	510 (162)

EPR analysis of the intermediate

Figure SI 17. X-band EPR experimental spectra (plain line) and simulations (dotted line) of the intermediate obtained using complex **1** placed at 0.25 mM in H_2O / 10% glycerol in the presence of 2 equivalents of Et_3N and 2 equivalents of H_2O_2. EPR parameters from simulation: $g_{//}$=2.249, $|A_{//}|$ = 510 MHz and $g_\perp$=2.066
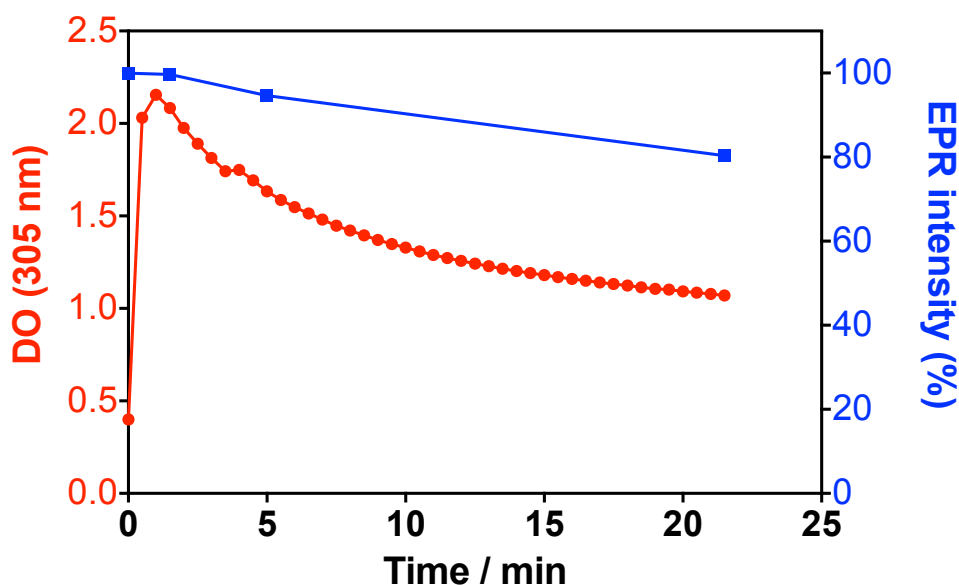
Evolution of of EPR intensity following the formation of the intermediate

Figure SI 18. Comparison of the evolution of the UV-Visible absorption at 305 nm (red) and the EPR intensity (blue) in the case of complex **1** at 0.5 mM in the presence of 50 mM of H_2O_2 (phosphate buffer pH 7 with 10% of glycerol).
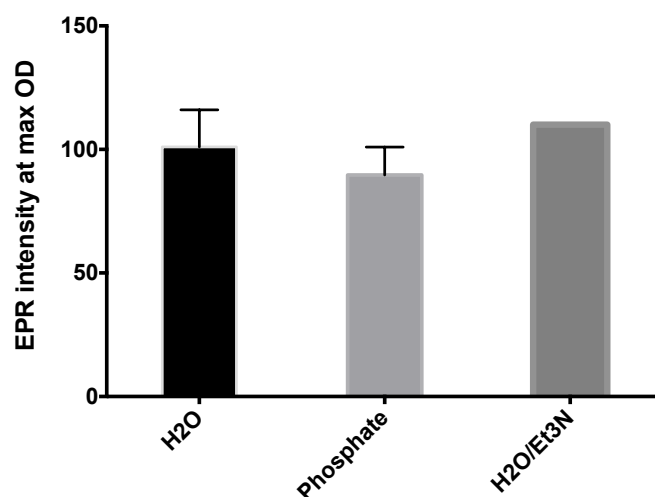
Figure SI 19. Relative EPR intensity (% of initial intensity) at the maximum formation of the intermediate after addition of H_2O_2 in different aqueous solutions (H_2O; Phosphate buffer set at pH 7, H_2O in the presence of Et_3N). [**1**]= 0.2-1 mM, [H_2O_2]=0.2-50 mM. The formation of **1-OOH** was followed by UV-visible absorption at 305 nm.

VI. DFT Calculations

Starting complexes

Given the high similarity between the two sets of ligands, DFT calculations were mainly conducted on the L^{AM}-based system.
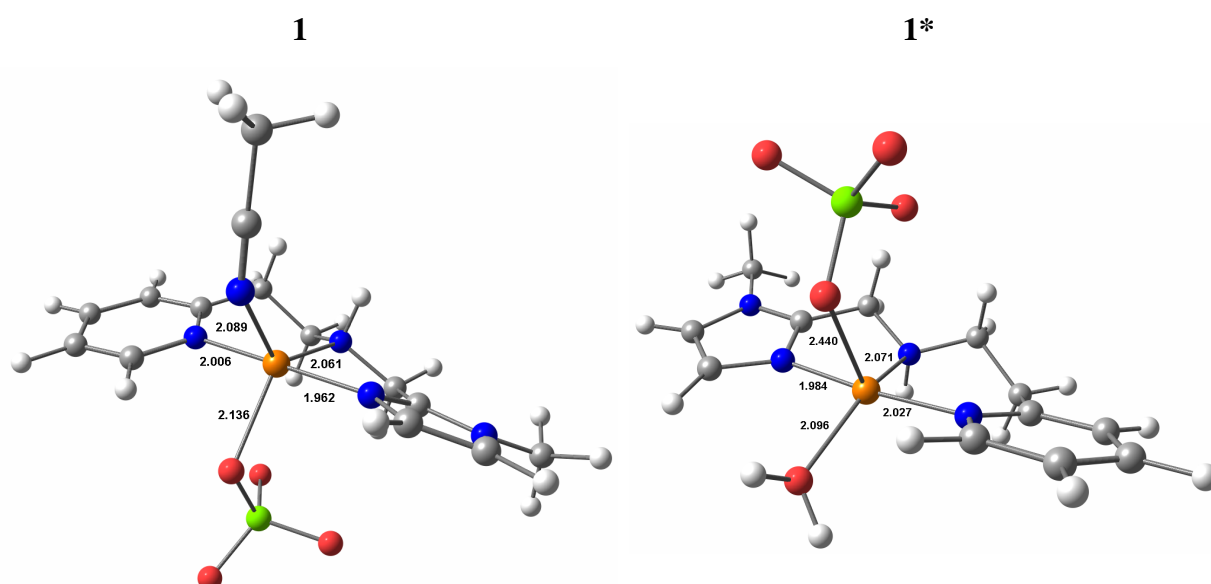

Figure SI 20. DFT-optimized structures and relevant metrical parameters of **1** and **1*.**

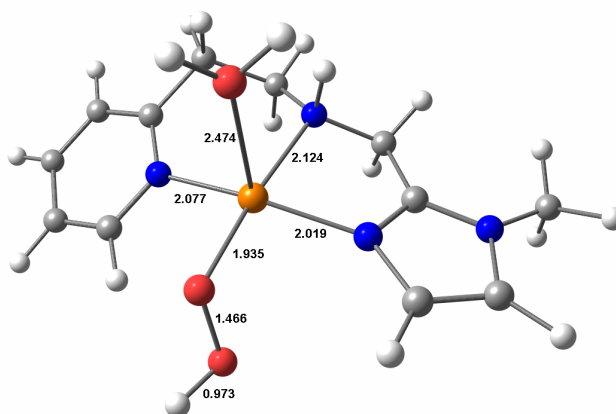***Different computed structures of the intermediate***

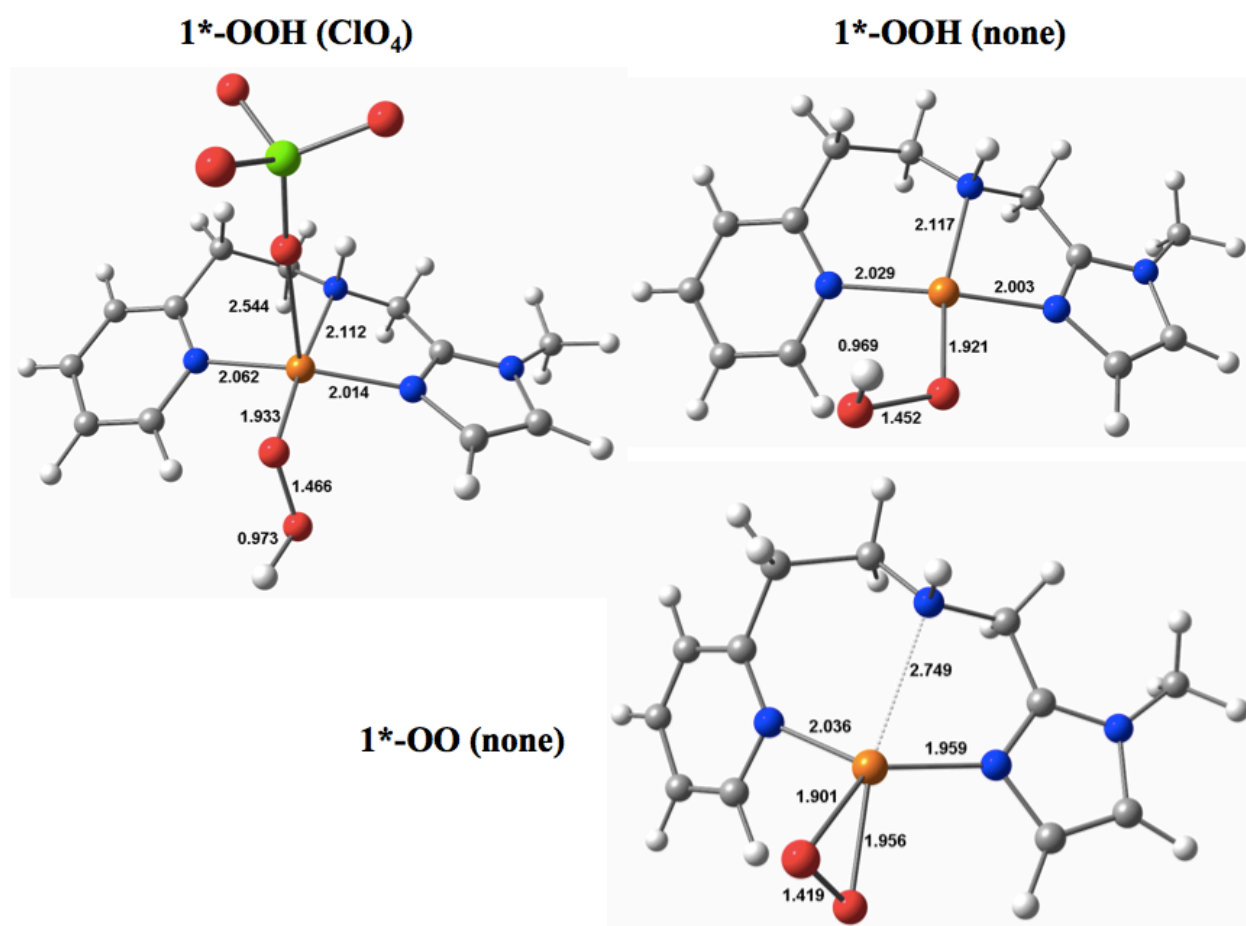Figure SI 21. DFT-optimized structure and relevant metrical parameters of **1*-OOH.**

Figure SI 22. Alternative DFT-optimized structures and relevant metrical parameters for the intermediate.
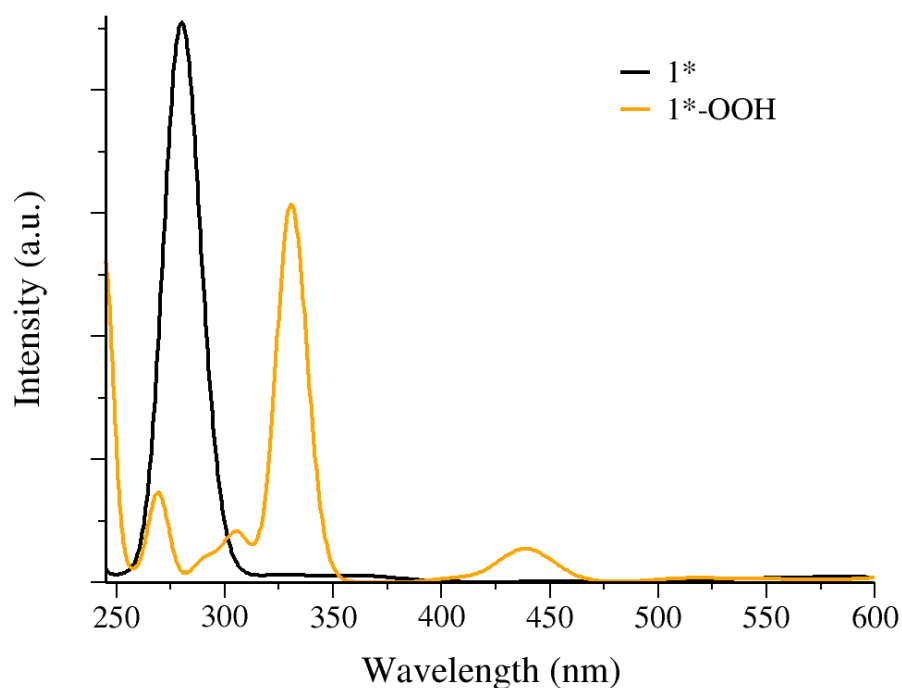
Computed spectroscopic and electronic properties

Figure SI 23 TDDFT-predicted UV-vis spectra of complexes **1*** (black line) and **1*-OOH** (orange line).
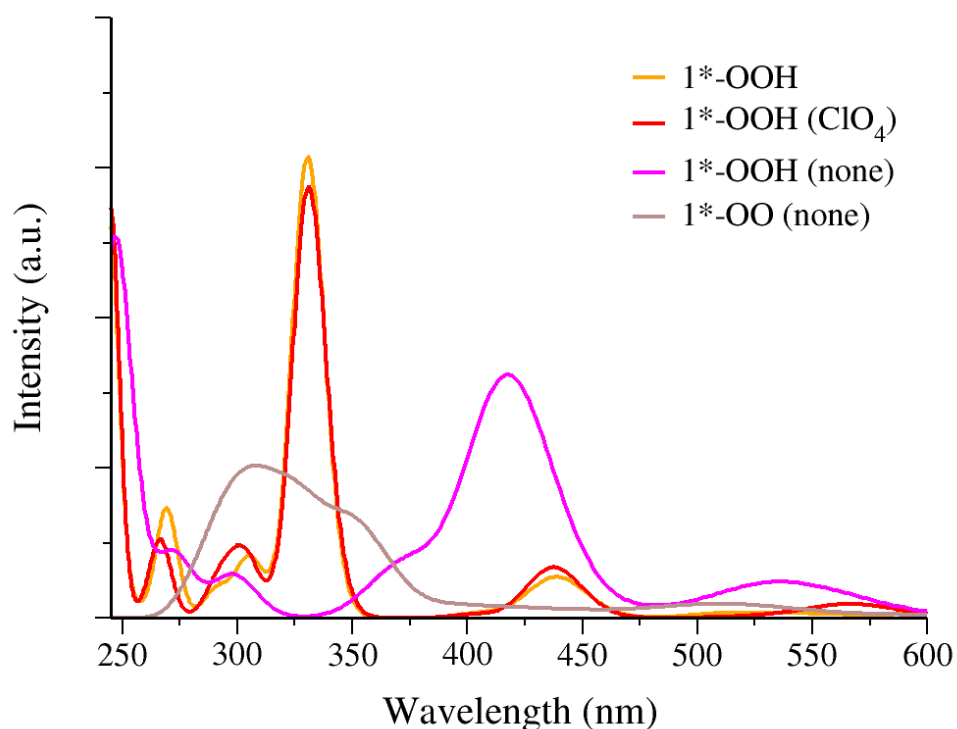

Figure SI 24 TDDFT-predicted UV-vis spectra of **1*-OOH** (orange line) and alternative intermediates (red, pink and brown lines). It is worth mentioning that the intermediate with one perchlorate and one hydroperoxo would also be a good model and that this structure cannot be excluded on the basis of our data.

Table S 5. TDDFT-calculated electronic transitions for complexes **1*** and **1*-OOH**.

Complex	λ^{calc} (nm)	f^{calc}	TDDFT assignment
1*	278	0.228	Ligand → Metal
1*-OOH	331	0.153	OOH → Metal
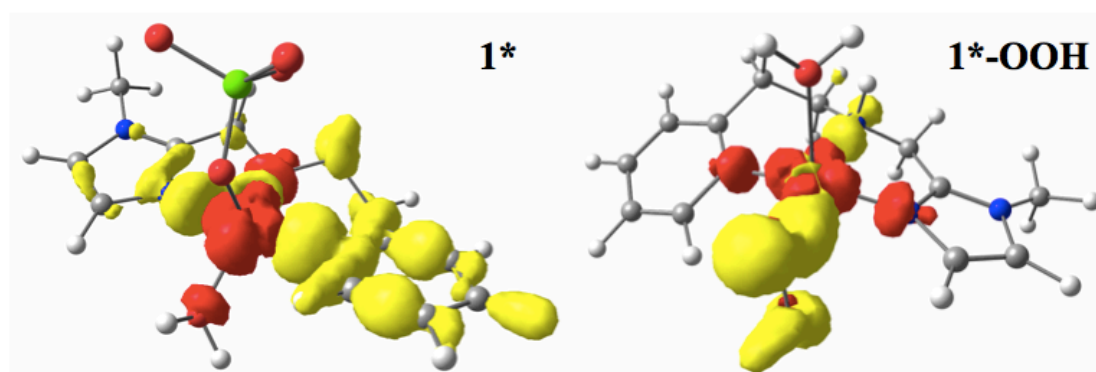
Figure SI 25 Difference electron density sketch for relevant transitions of complexes **1** and **1*-OOH** (yellow = negative, red = positive density).
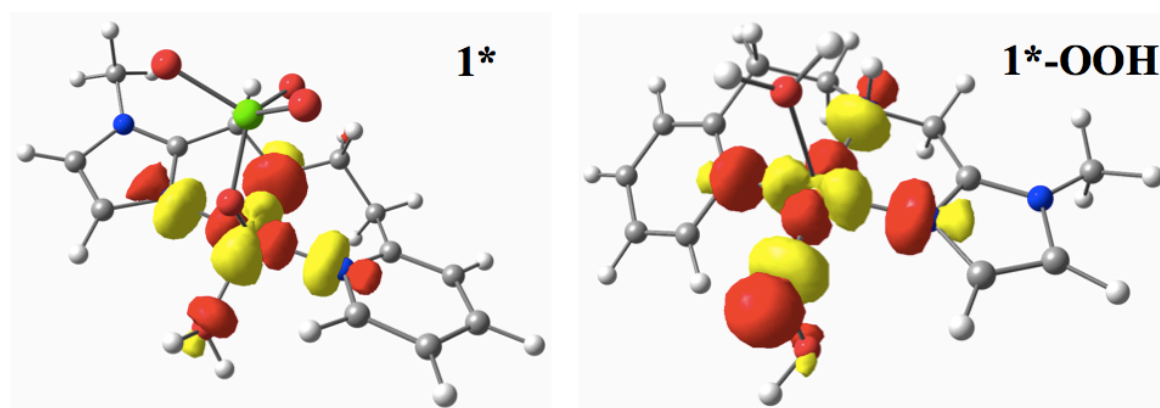
62% Cu, 3% O, 34% N, 1% remaining   **54% Cu, 26% O, 18% N, 2% remaining**

Figure SI 26. Localized SOMOs for complexes **1*** (left) and **1*-OOH** (right).

1*-OOH (ClO₄)
55% Cu, 26% O, 18% N, 1% remaining

1*-OOH (none)
49% Cu, 26% O, 24% N, 1% remaining

1*-OO (none)
34% Cu, 64% O, 1% N, 1% remaining
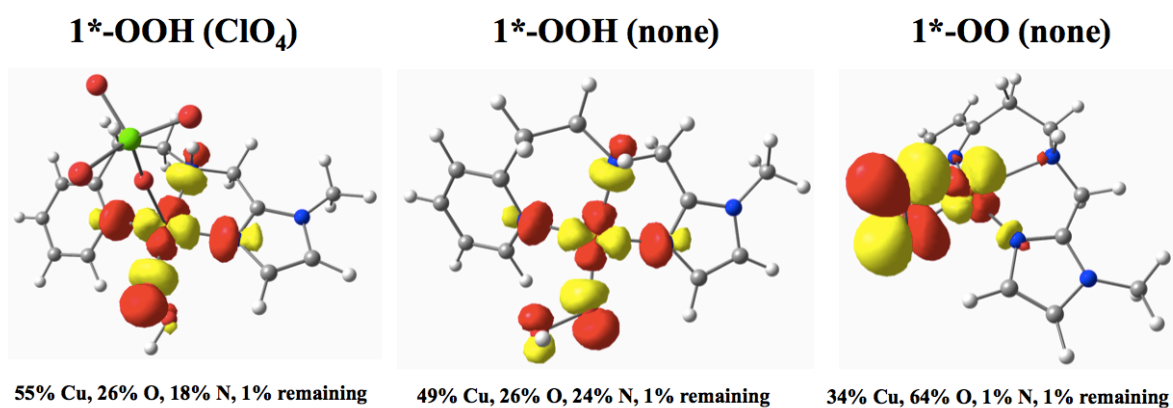
Figure SI 27. Localized SOMOs of alternative intermediates.

Table S 6. DFT-computed EPR parameters for complexes **1*** and **1*-OOH**.

Complex	g_{min}	g_{mid}	g_{max}	g_{iso}
1*	2.033	2.080	2.168	2.094
1*-OOH	2.030	2.058	2.136	2.075

Complex	$|A_{min}|$ (MHz)	$|A_{mid}|$ (MHz)	$|A_{max}|$ (MHz)
1*	20	202	450
1*-OOH	48	94	512

VII. References

[1] GM Sheldrick, A short history of SHELX, *Acta Cryst A*, **2008**, *64*, 112–122.

[2] NG Connelly, WE Geiger, Chemical Redox Agents for Organometallic Chemistry, *Chem Rev*, **1996**, *96*, 877–910

[3] Neese, F., The ORCA program system, *Wiley Interdiscip. Rev. Comput. Mol. Sci.* **2012**, *2*, 73-78.

[4] a) Perdew, J. P. Density-functional approximation for the correlation energy of the inhomogeneous electron gas, *Phys. Rev. B* 1**986**, *33*, 8822–8824; b) Perdew, J. P. Erratum: Density-functional approximation for the correlation energy of the inhomogeneous electron gas, *Phys. Rev. B* **1986**, *34*, 7406-7406; c) Becke, A. D. Density-functional exchange-energy approximation with correct asymptotic behavior, *Phys. Rev. A* **1988**, *38*, 3098-3100

[5] Neese, F. An improvement of the resolution of the identity approximation for the formation of the Coulomb matrix, *J. Comput. Chem.* **2003**, *24*, 1740-1747

[6] Weigend, F. Accurate Coulomb-fitting basis sets for H to Rn, *Phys. Chem. Chem. Phys.* **2006**, *8*, 1057-1065

[7] Pantazis, D. A.; Chen, X.-Y.; Landis, C. R.; Neese, F. All-Electron Scalar Relativistic Basis Sets for Third-Row Transition Metal Atoms, *J. Chem. Theory Comput.* **2008**, *4*, 908-919.

[8] Pantazis, D. A.; Neese, F. All-Electron Scalar Relativistic Basis Sets for the Lanthanides, *J. Chem. Theory Comput.* **2009**, *5*, 2229-2238

[9] a) Becke, A. A new mixing of Hartree–Fock and local density-functional theories, D. *J. Chem. Phys.* **1993**, *98*, 1372-1377; b) Lee, C. T.; Yang, W.T.; Parr, R. G. Development of the Colle-Salvetti correlation-energy formula into a functional of the electron density, *Phys. Rev. B* **1988**, *37*, 785-789

[10] Klamt, A.; Schürmann, G. COSMO: a new approach to dielectric screening in solvents with explicit expressions for the screening energy and its gradient, *J. Chem. Soc. Perkin Trans. 2* **1993**, 799-805

[11] a) Casida, M. E. Time-dependent density-functional response theory for molecules in Recent Advances in Density Functional Theory, Part I (Ed.: D. P. Chong), World Scientific, Singapore, **1995**; b) Stratmann, R. E.; Scuseria, G.E.; Frisch, M.J. An efficient implementation of time-dependent density-functional theory for
the calculation of excitation energies of large molecules, *J. Chem. Phys.* **1998**, *109*, 8218-8224; c) Bauernschmitt, R.; Ahlrichs, R. Treatment of electronic excitations within the

adiabatic approximation of time dependent density functional theory, *Chem. Phys. Lett.* **1996**, *256*, 454-464.

[12] a) Hirata, S.; Head-Gordon, M. Time-dependent density functional theory within the Tamm–Dancoff approximation, *Chem. Phys. Lett.* **1999**, *314*, 291-299; b) S. Hirata, M. Head-Gordon, Time-dependent density functional theory for radicals: An improved description of excited states with substantial double excitation character, *Chem. Phys. Lett.* **1999**, *302*, 375-382.

[13] Neese, F. Prediction of electron paramagnetic resonance g values using coupled perturbed Hartree–Fock and Kohn–Sham theory, *J. Chem. Phys.* **2001**, *115*, 11080-11080

[14] Chemcraft, http://chemcraftprog.com.

[15] An isostructural complex featuring a water molecule bound instead of acetonitrile has been previously reported (Kumar, P.; Kalita, A.; Mondal, B. Reduction of copper(II) complexes of tridentate ligands by nitric oxide and fluorescent detection of NO in methanol and water media, *Dalton Trans.* **2011**, *40*, 8656–8658).

[16] Westereng, B.; Wittrup Agger, J.; Horn, S.J.; Vaaje-Kolstad, G.; Aachmann, F.L.; Stenstrøm, Y.H. ; Eijsink, V.G.H.; Efficient separation of oxidized cello-oligosaccharides generated by cellulose degrading lytic polysaccharide monooxygenases. *J. Chromatogr. A*, **2013**, *1271*, 144-152